AGU PUBLICATIONS

Geophysical Research Letters

RESEARCH LETTER
10.1002/2016GL071094

Key Points:
- We present first measurements of solar wind plasma having interacted with the lunar nightside surface
- We observe two energetic neutral terminator cocentric rings, both of which originate in the solar wind bulk flow
- Our data provide the first observation indicative of a global solar zenith angle dependence of positive surface potentials

Correspondence to:
A. Vorburger,
vorburger@space.unibe.ch

Citation:
Vorburger, A., P. Wurz, S. Barabash, Y. Futaana, M. Wieser, A. Bhardwaj, M. B. Dhanya, and K. Asamura (2016), Transport of solar wind plasma onto the lunar nightside surface, *Geophys. Res. Lett.*, *43*, 10,586–10,594, doi:10.1002/2016GL071094.

Received 2 SEP 2016
Accepted 23 SEP 2016
Accepted article online 27 SEP 2016
Published online 19 OCT 2016

Transport of solar wind plasma onto the lunar nightside surface

A. Vorburger[1], P. Wurz[1], S. Barabash[2], Y. Futaana[2], M. Wieser[2], A. Bhardwaj[3], M. B. Dhanya[3], and K. Asamura[4]

[1]Physikalisches Institut, University of Bern, Bern, Switzerland, [2]Swedish Institute of Space Physics, Kiruna, Sweden, [3]Space Physics Laboratory, Vikram Sarabhai Space Center, Trivandrum, India, [4]Institute of Space and Astronautical Science, Sagamihara, Japan

Abstract We present first measurements of energetic neutral atoms that originate from solar wind plasma having interacted with the lunar nightside surface. We observe two distinct energetic neutral atom (ENA) distributions parallel to the terminator, the spectral shape, and the intensity of both of which indicate that the particles originate from the bulk solar wind flow. The first distribution modifies the dayside ENA flux to reach ~6° into the nightside and is well explained by the kinetic temperature of the solar wind protons. The second distribution, which was not predicted, reaches from the terminator to up to 30° beyond the terminator, with a maximum at ~102° in solar zenith angle. As most likely wake transport processes for this second distribution we identify acceleration by the ambipolar electric field and by the negatively charged lunar nightside surface. In addition, our data provide the first observation indicative of a global solar zenith angle dependence of positive dayside surface potentials.

1. Introduction

In recent years, the lunar dayside surface was proven to be very effective in neutralizing and reflecting impinging solar wind plasma: Up to 20% of the impinging solar wind protons are neutralized upon interaction with the lunar surface before being reflected back to space as hydrogen energetic neutral atoms (ENAs) [e.g., *McComas et al.*, 2009; *Wieser et al.*, 2009; *Vorburger et al.*, 2013; *Bhardwaj et al.*, 2015]. ENA imaging thus provides a powerful tool to investigate the solar wind plasma interaction process with the lunar surface.

Most previously published results on lunar ENAs have focused on the sunlit hemisphere of the Moon, where the solar wind plasma can reach the surface almost unhindered. Only one study on lunar nightside ENAs has so far been conducted [*Harada et al.*, 2014]. This study presented measurements taken when the Moon was located in Earth's magnetotail, though, and did thus not investigate the lunar surface interaction with the solar wind plasma but rather with Earth's plasma sheet.

It is known that, in contrast to solar photons, solar wind protons are to a certain extent accelerated into the lunar wake. This wake entry process has been studied in recent years during several missions. *Zhang et al.* [2014] presented ARTEMIS measurements in the lunar wake up to distances of 12 lunar radii (far-Moon wake). Their measurements showed that the solar wind plasma is accelerated into the lunar wake structure through the pressure gradient force and the ambipolar electric field. Plasma entry into the near-Moon wake (~100–200 km above the surface) was recently observed by KAGUYA/SELENE, Chang'E-1, and Chandrayaan-1. The lunar wake plasma penetration observations by SELENE were conducted by MAP, the MAgnetic field and Plasma experiment. The protons measured by MAP are thought to have been accelerated into the near-Moon wake by the bipolar electric field around the wake boundary [*Nishino et al.*, 2009a] and by scattering from the dayside followed by solar wind motional electric field pickup [*Saito et al.*, 2008; *Nishino et al.*, 2009b]. *Wang et al.* [2010] reported on accelerated particles observed by the Solar Wind Ion Detectors on board the Chang'E-1 spacecraft. These ions are also proposed to originate in scattered solar wind protons, which have been accelerated into the lunar wake by the convection electric field of the solar wind and the $\vec{E}\times\vec{B}$ drift in the ambipolar electric field at the flank of the lunar wake. The Sub-keV Atom Reflecting Analyzer (SARA) instrument onboard Chandrayaan-1 also measured ions in the near-Moon wake, the origin of most of which have been identified (including diffusion of solar wind protons into the wake along the interplanetary magnetic field (IMF),

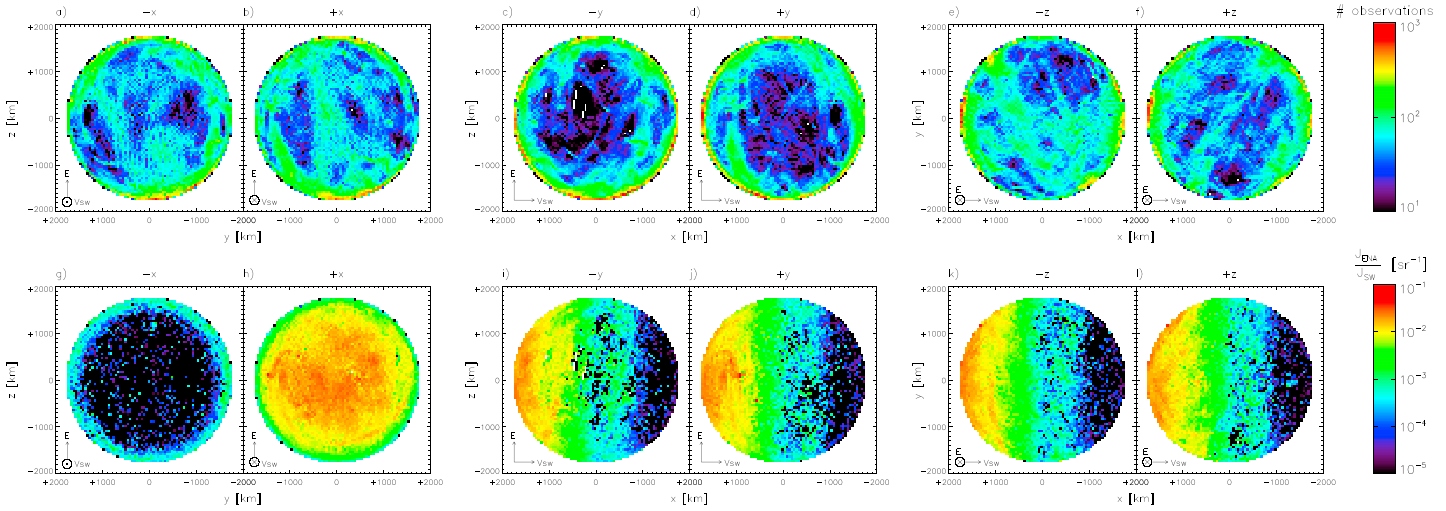

Figure 1. Projections of lunar ENA observations. Number of observations and differential ENA flux divided by the number of observations and the solar wind flux in (sr^{-1}). (a, g) The projection of the $-x$ hemisphere (i.e., lunar nightside). (b, h) The projection of the $+x$ hemisphere (i.e., lunar dayside). (c, i) The projection of the $-y$ hemisphere. (d, j) The projection of the $+y$ hemisphere. (e, k) The projection of the $-z$ hemisphere. (f, l) The projection of the $+z$ hemisphere. For convenience, the direction of the solar wind flow and the direction of the convective electric field are depicted in all panels.

Larmor motion, and dayside scattering), but the origin of some of which still remains unclear [*Futaana et al.*, 2010; *Dhanya et al.*, 2013, 2016].

We will present measurements from a third region of the lunar wake, namely, of protons that enter the Moon's wake at such close distance so that they can interact with the lunar nightside surface. Solar wind protons hitting the lunar nightside surface have been known to exists since the Apollo missions, where ion bursts deep in the lunar night were observed by surface deployed superthermal ion detectors [*Freeman Jr.*, 1972].

2. Instrumentation and Observations

For this study we analyzed measurements conducted by the Chandrayaan-1 Energetic Neutrals Analyzer (CENA) [*Kazama et al.*, 2007], which is a part of the SARA instrument [*Bhardwaj et al.*, 2005; *Barabash et al.*, 2009] onboard Chandrayaan-1 [*Goswami and Annadurai*, 2009]. CENA measured ENAs originating from the lunar surface within the energy range 10 eV to 3.3 keV and an energy resolution of $\Delta E/E \sim 50\%$. CENA's field of view consists of seven angular sectors (five of which are purely surface pointing), with surface-projected footprints of approximately 100–400 km × 10–20 km, depending on the sector number and spacecraft altitude. For this analysis, we only used neutral hydrogen measurements in the energy range 10 eV to 2.2 keV, measured at both of Chandrayaan-1's operational altitudes of 100 km and 200 km when the Moon was located upstream of the terrestrial bow shock, i.e., was fully exposed to the solar wind plasma.

When analyzing dayside ENA measurements, we corrected for CENA's viewing direction, i.e., the fact that we sample only part of the 2π scattering function. Unfortunately, determination of such a scattering function for the nightside is not possible, since the solar wind incidence angle as a function of lunar longitude and latitude is not known for the nightside. We thus present the data as observed in physical units.

CENA's full data product provided us with 168 upstream orbits to be analyzed, each of which provides about 2 h of data (1 h of which is spent on the nightside) for each of the five angular sectors, with an integration time for an individual measurement of 4 s. Our full analysis thus contains on the order of 1 million individual measurements. Solar wind and IMF conditions used in this study were taken from the Wind and ACE missions, the data products of both of which were time shifted to account for the distance between Chandrayaan-1 and the respective spacecraft. During CENA's operational periods, the solar wind velocity ranged from ~250 km s^{-1} to ~560 km s^{-1}, with a mean of ~370 km s^{-1} and a standard deviation of ~78 km s^{-1}. The solar wind proton and electron thermal velocity distributions had a mean of ~29 km s^{-1} and ~2167 km s^{-1}, respectively, with corresponding standard deviations of ~11 km s^{-1} and ~378 km s^{-1}. The IMF strength ranged from almost 0 to ~12 nT, with a mean of ~4 nT and a standard deviation of ~2 nT.

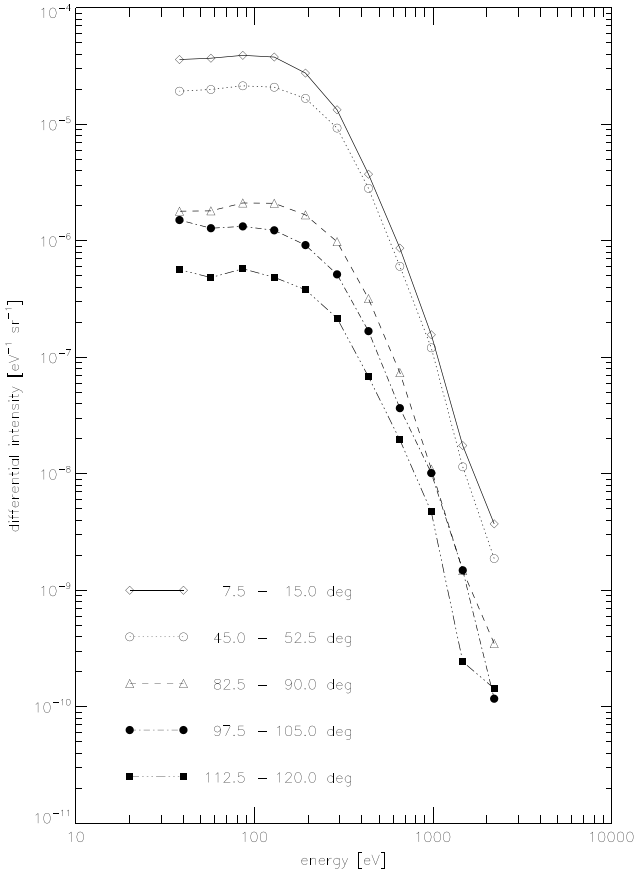

Figure 2. Five solar wind normalized ENA energy spectra. The curves with empty symbols correspond to ENA populations from the dayside surface, whereas the curves with filled symbols belong to ENA populations coming from the nightside surface. The annotations denote from which solar zenith angle intervals the energy spectra were taken.

3. Results

The coordinate system within which the data are presented is optimized to analyze the lunar wake plasma entry process. The origin of the system is set at the center of the Moon. The x direction points toward the Sun, i.e., points toward the antisolar wind velocity ($-\vec{v}_{sw}$), the z direction is along the solar wind convection electric field ($\vec{E} = -\vec{v}_{sw} \times \vec{B}_{IMF}$), and the y direction completes the right-hand system. In this coordinate system, the IMF is confined to the x–y plane with the y component always positive. Aberration due to both the Moon's orbital motion and ACE's velocity was corrected for. As a compromise between field of views' wide opening angles in azimuth direction and narrow opening angles in elevation direction, the projected field of view was chosen to be 50 km. This is justified by the sensor having an angular response resembling a Gaussian function and thus being more sensitive to particles coming from the nadir direction [*Vorburger*, 2013].

Figure 1 presents the projection of the lunar hydrogen ENA observations onto the y–z, the x–z, and the x–y planes. Figures 1a–Figure 1f depict the number of 4 s observations on a logarithmic scale. Figures 1g–Figure 1l show the hydrogen differential ENA flux divided by the number of observations and the solar wind flux. In this kind of projection Figure 1g shows the lunar nightside and Figure 1h shows the lunar dayside. For Figures 1i to 1l the Sun is located to the left. All panels contain arrows showing the direction of the solar wind flow ($\vec{v}_{sw} = (v_{sw}, 0, 0)$) and the direction of the convection electric field ($\vec{E} = (0, 0, E)$). It is obvious from Figure 1g that ENAs are not strictly confined to the lunar dayside surface: there is a substantial amount of ENAs coming from just beyond the terminator, which form a wide ring structure parallel to the terminator.

To determine the origin of these nightside ENAs, we first analyzed their energy spectra. In a previously published paper, *Futaana et al.* [2012] analyzed the energy spectra of dayside ENAs also measured by CENA. They showed that the individual energy spectra are well reproduced by a Maxwell-Boltzmann distribution function and that the characteristic energy of dayside ENAs is directly proportional to the solar wind velocity.

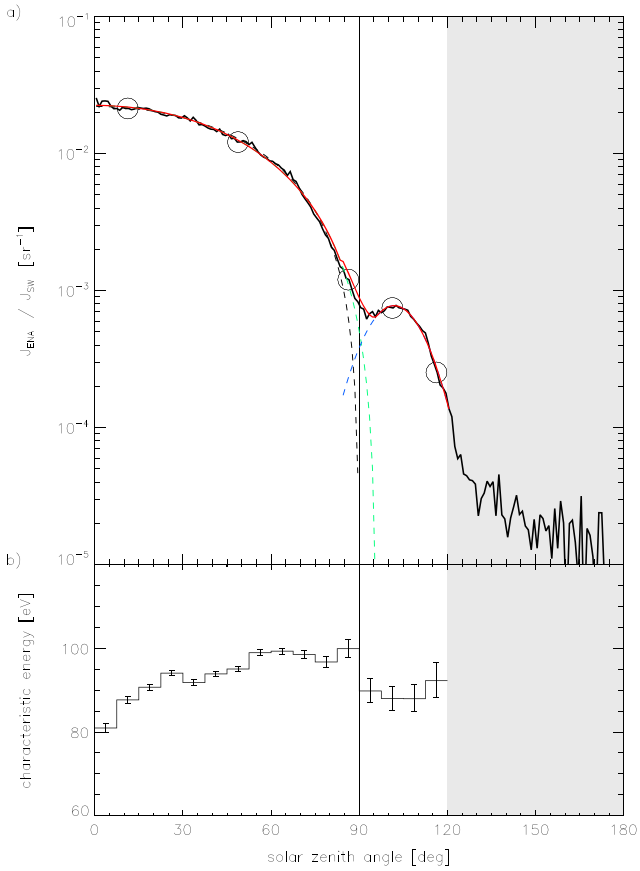

Figure 3. (a) Solar wind normalized differential ENA flux and (b) characteristic energy versus solar zenith angle. Figure 3a also shows four theoretical curves, added to guide the reader's eye. The black dashed curve shows a cosine which tends toward zero at the terminator. The green dashed curve is a modified version of the black curve that tends toward zero ~6° beyond the terminator. The blue dashed curve shows a Gaussian distribution with a maximum at ~102° and a full width half max of ~30°. The red curve is the sum of the green and the blue curves. In Figure 3b, the 5% and 95% percentiles are shown by the vertical bars. For convenience, a solid black line representing the terminator is shown in both panels. The shaded area right of ~120° denotes the region where the characteristic energy spectra resemble the one-count level. Also depicted in Figure 3a are five regions for which the energy spectra are shown in Figure 2.

Figure 2 shows a few sample energy spectra for ENAs belonging to the dayside as well as the near nightside. In their paper, *Futaana et al.* [2012] mention that there is no reliable detection efficiency of the CENA instrument available below 25 eV. We thus only used ENAs with energies ≥38 eV (the next energy bin after 25 eV) when determining the characteristic energy as well. Figure 2 shows that not only the dayside ENA energy spectra (curves with open symbols) are well represented by a Maxwell-Boltzmann distribution function but also that the nightside energy spectra (curves with filled symbols) closely resemble the dayside energy spectra and that they are thus also well represent by a Maxwell-Boltzmann distribution.

To see how far the solar wind plasma is transported beyond the terminator, we plotted the solar wind normalized differential hydrogen ENA flux versus solar zenith angle in Figure 3a. This figure shows the data in the lunar solar ecliptic coordinate system, which is independent of ACE and Wind satellite data. In this coordinate system 0° corresponds to the subsolar point, 90° corresponds to the terminator, and 180° corresponds to the antisubsolar point. If the Moon-solar wind interaction was purely a geometrical problem, the ENA flux would tend toward zero at the terminator and remain zero on the nightside (black dashed lines). This is not the case; though, we observe two distinct nightside ENA populations. The first population results in the ENA flux reaching ~6° beyond the terminator (green dashed line). The second population starts to dominate shortly after the terminator, reaches ~30° into the nightside, and has a maximum at ~102° (blue dashed line). The pure nightside ENA flux (ENAs coming from 90° to ~120° in solar zenith angle) amounts to ~1.5% of the total dayside flux. The flux and energy profile of the ENAs coming from the far nightside (beyond 120°; shaded area)

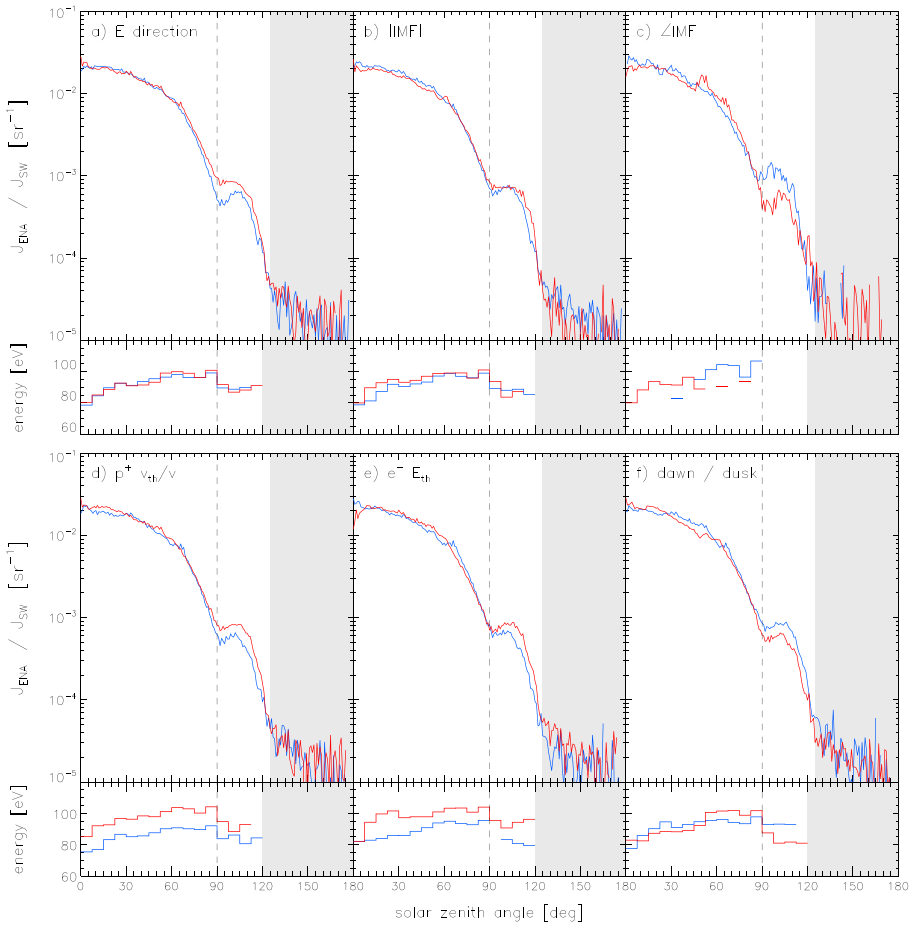

Figure 4. Solar wind normalized differential ENA flux grouped according to (a) $\vec{E}$ direction (negative $\vec{E}$ hemisphere (blue) and positive $\vec{E}$ hemisphere (red)), (b) IMF magnitude (<5 nT (blue) and >5 nT (red)), (c) angle between the IMF and the solar wind bulk flow (<30° (blue) and >150° (red)), (d) ratio of proton thermal speed to solar wind speed (<1:15 (blue) and >1:15 (red)), (e) electron thermal energy (<12.5 eV (blue) and >12.5 eV (red)), (f) and dawn/dusk hemisphere (blue/red).

is very low and resembles the one-count level. These ENAs were therefore not further analyzed. Figure 3a also shows, for convenience, the locations for which energy spectra are shown in Figure 2) with circles.

Having analyzed the dependency of the ENA flux on the solar zenith angle, we also analyzed the dependency of the characteristic ENA energy on the solar zenith angle. The result of this analysis is shown in Figure 3b, where the horizontal bars depict the characteristic energy for a given solar zenith angle interval and where the vertical bars depict the 95 percentiles, determined by applying a resampling bootstrap algorithm with a sample number of 100,000. As one can see from this panel, there is a steady increase in characteristic energy with increasing solar zenith angle on the lunar dayside. At the terminator, though, there is an abrupt drop of ~10 eV in characteristic energy, and the characteristic energy stays more or less constant on the lunar nightside but exhibits much larger variation than the dayside ENAs. Overall, the characteristic energy of the nightside ENAs is on average 4 eV lower than the characteristic energy of the dayside ENAs.

To analyze which processes govern the solar wind plasma transport onto the lunar nightside, we analyzed the flux and energy profiles for different solar wind plasma conditions. These conditions include the following: (i) solar wind speed, (ii) proton thermal speed, (iii) electron thermal speed, (iv) IMF magnitude, (v) IMF direction, (vi) $\vec{E}$ direction, and (vii) dawn/dusk hemisphere. The ENA flux and characteristic energy profiles that exhibited a dependency on one of the plasma conditions mentioned above are shown in Figure 4. The conditions are as follows: $\vec{E}$ direction (negative $\vec{E}$ hemisphere (blue) and positive $\vec{E}$ hemisphere (red); Figure 4a), IMF magnitude (<5 nT (blue) and >5 nT (red); Figure 4b), angle between the IMF and the solar wind bulk flow (<30° (blue) and >150° (red); Figure 4c), ratio of proton thermal speed to solar wind speed (<1:15 (blue) and >1:15 (red);

Figure 4d), electron thermal energy (<12.5 eV (blue) and >12.5 eV (red); Figure 4e), and dawn/dusk hemisphere (blue/red; Figure 4f). Note that for some plasma conditions and solar zenith intervals the statistics were not sufficient enough to determine a definite characteristic energy from the energy spectra. In that case, no line is shown. It is also important to note, here, that many of these parameters are correlated. To resolve which of two correlated parameters is responsible for an observed effect, it would be necessary to vary one parameter while the other parameter remains constant. Unfortunately, due to the limited number of observations and the rather constant nature of the solar wind plasma during the observations, such an analysis was impossible here.

4. Discussion

The dayside ENA flux arising from the solar wind plasma has been thoroughly studied in recent years [e.g., *Vorburger et al.*, 2012, 2013; *Futaana et al.*, 2012]. We derive from our measurements characteristic dayside ENA energies ranging from ~80 eV to ~100 eV, with a mean of ~94 eV (cf. Figure 3b). This is in good agreement with the values presented by *Futaana et al.* [2012], who computed from 108 dayside measurements a median of 93 eV and 25% and 75% percentiles of 81.7 eV and 111 eV, respectively. The dayside characteristic energy steadily increases with increasing solar zenith angle, most probably as a result of variation in dayside surface charging. At the subsolar point, the lunar surface has a potential of a few (tens of) volts, and it decreases with increasing solar zenith angle up to ~ 80°, where it rapidly becomes negative [cf. *Stubbs et al.*, 2014]. Since a positive surface potential decelerates and a negative surface potential accelerates the impinging solar wind ions, ions reaching the subsolar point are expected to have lower energies than ions arriving closer to the terminator, which agrees well with the trend we observe in our dayside data. Our data thus provide the first observation indicative of a global solar zenith angle dependence of positive dayside surface potentials.

At the terminator we observe a 10 eV step in characteristic ENA energy (cf. Figure 3b), from which we infer a change in proton energy of about 100 eV [cf. *Futaana et al.*, 2012]. Most processes known to transport solar wind protons into the lunar wake add, rather than subtract, energy. There has only been one observation where protons were decelerated when entering the lunar wake. These observations were presented by *Nishino et al.* [2009a], who showed that the solar wind protons gain kinetic energy in one hemisphere, while they lose energy in the other hemisphere, probably due to proton Larmor motions and inward electric fields around the wake boundary. The determining factor in which hemisphere gains and which hemisphere loses energy was identified as the direction of the y component of the IMF. With the convection electric field being the cross product between the solar wind velocity and the IMF, such an IMF y component asymmetry should in our analysis show up as an $\vec{E}$ hemisphere asymmetry. Figure 4a shows the division of the data set into the positive and negative $\vec{E}$ hemispheres. Whereas there is an ENA flux asymmetry in the nightside data for the two hemispheres, the energy spectra are virtually the same. We thus doubt that the energy loss we observe at the terminator has the same cause as the energy loss observed by *Nishino et al.* [2009a]. Not being aware of any other processes that could decelerate protons upon entry into the near-lunar wake, this 10 eV drop in characteristic ENA energy at the terminator is currently not understood. It is currently also not understood why there is more flux in the positive $\vec{E}$ hemisphere. With the $\vec{E}$ field accelerating protons in the positive direction, one would expect solar wind protons to be drawn farther into the Southern than into the Northern Hemisphere.

In the lunar wake, we observe two populations of lunar nightside ENAs (cf. Figure 3a). The first population (green curve in Figure 3a) modifies the dayside ENA flux to reach ~6° beyond the lunar terminator and arises from the kinetic temperature of the solar wind (see discussion below), which allows the protons to access surface locations up to a few degrees behind the geometric shadow. The second population is ENAs from farther into the nightside (blue curve in Figure 3a). With the locations being too far into the nightside to be explained by kinetic temperature effects, plasma processes need to direct protons to these locations on the nightside. The red curve, which is the sum of the green and the blue curves, shows that the complete ENA flux is well reproduced by these two curves.

The nightside ENAs have an energy spectrum closely resembling the dayside energy spectrum (cf. Figure 2). For the same reasoning as presented in *Futaana et al.* [2012] we can conclude that the nightside ENAs do not originate from the lunar surface material (and are thus not sputtered particles, which would have much lower energies [*Wurz et al.*, 2007]) but must be reflected and neutralized solar wind ions. But in contrast to the dayside ENAs, which are a result of solar wind protons interacting directly with the lunar surface, the nightside ENAs stem from solar wind protons that have been processed by some means. *Futaana et al.* [2012]

also showed that the characteristic dayside ENA energy is proportional to the solar wind velocity and that the dayside ENAs usually posses approximately 10% of the impinging solar wind proton energy. This statement is also true for lunar nightside ENAs.

Figure 4 shows that whereas the IMF magnitude has a minimal influence on the nightside ENA generation (except for maybe some broadening of the ring; Figure 4b), there is a noticeable difference in the ENA flux of the nightside when the IMF was quasi-parallel (blue) and when the IMF was quasi-antiparallel (red) to the solar wind bulk velocity. This difference decreases with increasing angle and has completely vanished when the IMF is perpendicular to the solar wind bulk velocity. This might be favoring of diffusion of solar wind protons parallel to diffusion antiparallel to the IMF, which was also observed in lunar protons measured by SARA's ion sensor and presented by *Dhanya et al.* [2016].

The solar wind kinetic temperature adds a perpendicular velocity component to the (much larger) parallel velocity component. This perpendicular component amounts on average to ~5–10% of the total velocity and thus allows for the solar wind ions to reach ~5° into the nightside (for pure geometric reasons). As the ratio between the perpendicular and the parallel component increases, particles arrive at steeper angles and are thus able to penetrate farther into the lunar nightside. Figure 4d) shows the separation of the data set into small/large ratios of perpendicular to parallel velocity components, where indeed protons with larger ratios are able to penetrate farther into the lunar nightside than protons with smaller ratios. In addition, the characteristic energy of the ENAs with larger ratio is distinctly larger than the characteristic energy of the ENAs with smaller ratios.

Another process often associated with lunar plasma wake penetration is acceleration by the ambipolar electric field [c.f. *Samir et al.*, 1983; *Ogilvie et al.*, 1996; *Halekas et al.*, 2005; *Farrell et al.*, 2008; *Halekas et al.*, 2011]. The ambipolar electric field is a result of electrons having higher thermal velocities than protons, which makes them diffuse into the vacuum of the lunar wake ahead of the protons. This in turn generates an electric field pointing toward the wake and thus accelerates protons toward the lunar nightside surface. This electric field is symmetric along the terminator, with the field strength being proportional to the electron thermal energy [c.f. *Kallio*, 2005]. Figure 4e shows that indeed protons are able to penetrate deeper into the lunar nightside when the electron thermal energy was high rather than low. As in Figure 4d, there is a distinct difference in characteristic energy for the two groups, with the characteristic energy being larger in the high-electron thermal energy case.

A further asymmetry discernible in our measurements concerns the local time of the proton surface interaction: There is more flux coming from the dawn than from the dusk hemisphere, and the characteristic energy step at the terminator is only well pronounced on the dusk hemisphere and is practically nonexistent on the dawn hemisphere. This dawn/dusk asymmetry might either be associated with plasma physics processes or with the fact that the lunar surface at the dusk side has just spent approximately 14 days at ~100 K, which is expected to have altered the lunar surface backscattering properties to some degree.

5. Summary and Conclusion

We presented first measurements of lunar wake ENAs resulting from solar wind plasma interacting with the lunar nightside surface. There are two distinct populations of nightside ENAs, amounting together to ~1.5% of the total dayside flux. The first population reaches ~6° beyond the terminator and is well explained by the kinetic temperature of the solar wind. The second population reaches from the terminator to ~120° in solar zenith angle, with a maximum at ~102°. The average characteristic energy of the nightside ENAs is ~4 eV lower than the average dayside population, probably due to plasma deceleration. It still closely resembles the spectral shape of the dayside energy spectrum though. We conclude that the nightside ENAs also originate in the solar wind bulk flow.

Analysis of possible plasma condition influences shows that the protons responsible for the observed nightside ENAs were most probably guided to the nightside by kinetic temperature effects and by the ambipolar electric field, with possible contributions from the negative charging of the lunar nightside. In addition, there seems to be a favoring of diffusion parallel to diffusion antiparallel to the IMF and either a plasma transport or surface reflection alteration effect associated with the local lunar time. Having not observed any strong correlation with the IMF strength or direction, plasma entry by gyromotion, scattering, or high-energy tail effects cannot have played a major role in transporting the protons responsible for these ENAs to the lunar nightside.

In addition, our lunar dayside data show a steady increase in characteristic ENA energy with increasing solar zenith angle. These are the first observations indicative of a global solar zenith angle dependence of positive dayside surface potentials.

The Moon offers a natural laboratory to study plasma physics interaction with planetary surfaces, and ENA imaging offers a suitable tool to investigate such processes. Our measurements show that solar wind plasma can effectively be transported into the lunar wake and onto the lunar nightside surface, where the plasma is neutralized upon interaction. Similar processes are expected to take place on other airless bodies, e.g., Mercury, the Galilean moons, asteroids, dormant comets, and other objects without an atmosphere.

Acknowledgments
Solar wind parameters from the Wind and ACE spacecrafts were used as a reference for this study. The authors thank K.W. Ogilvie and A.J. Lazarus for providing Wind data as well as N.F. Ness and D. McComas for providing ACE data. The efforts at Space Physics Laboratory, Vikram Sarabhai Space Centre, are supported by Indian Space Research Organisation (ISRO). All data used for this study can be obtained upon request (vorburger@space.unibe.ch).

References

Barabash, S., et al. (2009), Investigation of the solar wind-Moon interaction onboard Chandrayaan-1 mission with the SARA experiment, *Curr. Sci.*, *96*(4), 526–532.

Bhardwaj, A., S. Barabash, Y. Futaana, Y. Kazama, K. Asamura, R. Sridharan, M. Holmström, P. Wurz, and R. Lundin (2005), Low energy neutral atom imaging on the Moon with the SARA instrument aboard Chandrayaan-1 mission, *J. Earth Syst. Sci.*, *114*(6), 749–760, doi:10.1007/BF02715960.

Bhardwaj, A., et al. (2015), A new view on the solar wind interaction with the Moon, *Geosci. Lett.*, *2*(10), 1–15, doi:10.1186/s40562-015-0027-y.

Dhanya, M. B., A. Bhardwaj, Y. Futaana, S. Fatemi, M. Holmström, S. Barabash, M. Wieser, P. Wurz, A. Alok, and R. S. Thampi (2013), Proton entry into the near-lunar plasma wake for magnetic field aligned flow, *Geophys. Res. Lett.*, *40*, 2913–2917, doi:10.1002/grl.50617.

Dhanya, M. B., A. Bhardwaj, Y. Futaana, S. Barabash, A. Alok, M. Wieser, M. Holmström, and P. Wurz (2016), Characteristics of proton velocity distribution functions in the near-lunar wake from Chandrayaan-1/SWIM observations, *Icarus*, *271*, 120–130, doi:10.1016/j.icarus.2016.01.032.

Farrell, W. M., T. J. Stubbs, J. S. Halekas, G. T. Delory, M. R. Collier, R. R. Vondrak, and R. P. Lin (2008), Loss of solar wind plasma neutrality and affect on surface potentials near the lunar terminator and shadowed polar regions, *Geophys. Res. Lett.*, *35*, L05105, doi:10.1029/2007GL032653.

Freeman Jr., J. W. (1972), Energetic ion bursts on the nightside of the Moon, *J. Geophys. Res.*, *77*, 239–243, doi:10.1029/JA077i001p00239.

Futaana, Y., S. Barabash, M. Wieser, M. Holmström, A. Bhardwaj, M. B. Dhanya, R. Sridharan, P. Wurz, A. Schaufelberger, and K. Asamura (2010), Protons in the near-lunar wake observed by the Sub-keV Atom Reflection Analyzer on board Chandrayaan-1, *J. Geophys. Res.*, *115*, A10248, doi:10.1029/2010JA015264.

Futaana, Y., S. Barabash, M. Wieser, M. Holmström, C. Lue, P. Wurz, A. Schaufelberger, A. Bhardwaj, M. Dhanya, and K. Asamura (2012), Empirical energy spectra of neutralized solar wind proton from the lunar regolith, *Geophys. Res. Lett.*, *117*, E05005, doi:10.1029/2011JE004019.

Goswami, J., and M. Annadurai (2009), Chandrayaan-1: India's first planetary science mission to the Moon, *Curr. Sci.*, *96*(4), 486–491.

Halekas, J. S., S. D. Bale, D. L. Mitchell, and R. P. Lin (2005), Electrons and magnetic fields in the lunar plasma wake, *J. Geophys. Res.*, *110*, A07222, doi:10.1029/2004JA010991.

Halekas, J. S., Y. Saito, G. T. Delory, and W. M. Farrell (2011), New views of the lunar plasma environment, *Planet. Space Sci.*, *59*, 1681–1694, doi:10.1016/j.pss.2010.08.011.

Harada, Y., et al. (2014), Backscattered energetic neutral atoms from the Moon in the Earth's plasma sheet observed by Chandarayaan-1/Sub-keV Atom Reflecting Analyzer instrument, *J. Geophys. Res. Space Physics*, *119*, 3573–3584, doi:10.1002/2013JA019682.

Kallio, E. (2005), Formation of the lunar wake in quasi-neutral hybrid model, *Geophys. Res. Lett.*, *32*, L06107, doi:10.1029/2004GL021989.

Kazama, Y., S. Barabash, M. Wieser, K. Asamura, and P. Wurz (2007), Development of an LENA instrument for planetary missions by numerical simulations, *Planet. Space Sci.*, *55*, 1518–1529, doi:10.1016/j.pss.2006.11.027.

McComas, D., et al. (2009), Lunar backscatter and neutralization of the solar wind: First observations of neutral atoms from the Moon, *Geophys. Res. Lett.*, *36*, L12104, doi:10.1029/2009GL038794.

Nishino, M. N., et al. (2009a), Pairwise energy gain-loss feature of solar wind protons in the near-Moon wake, *Geophys. Res. Lett.*, *36*, L12108, doi:10.1029/2009GL039049.

Nishino, M. N., et al. (2009b), Solar-wind proton access deep into the near-Moon wake, *Geophys. Res. Lett.*, *36*, L16103, doi:10.1029/2009GL039444.

Ogilvie, K. W., J. T. Steinberg, R. J. Fitzenreiter, C. J. Owen, A. J. Lazarus, W. M. Farrell, and R. B. Torbert (1996), Observations of the lunar plasma wake from the WIND spacecraft on December 27, 1994, *Geophys. Res. Lett.*, *23*, 1255–1258, doi:10.1029/96GL01069.

Saito, Y., et al. (2008), Solar wind proton reflection at the lunar surface: Low energy ion measurement by MAP-PACE onboard SELENE (KAGUYA), *Geophys. Res. Lett.*, *35*, L24205, doi:10.1029/2008GL036077.

Samir, U., K. H. Wright, and N. H. Stone Jr. (1983), The expansion of a plasma into a vacuum: Basic phenomena and processes and applications to space plasma physics, *Rev. Geophys. Space Phys.*, *21*, 1631–1646, doi:10.1029/RG021i007p01631.

Stubbs, T. J., W. M. Farrell, J. S. Halekas, J. K. Burchill, M. R. Collier, M. I. Zimmerman, R. R. Vondrak, G. T. Delory, and R. F. Pfaff (2014), Dependence of lunar surface charging on solar wind plasma conditions and solar irradiation, *Planet. Space Sci.*, *90*, 10–27, doi:10.1016/j.pss.2013.07.008.

Vorburger, A. (2013), Investigation of the Solar Wind Interaction with the Lunar Surface, Univ. Bern, Switzerland.

Vorburger, A., P. Wurz, S. Barabash, M. Wieser, Y. Futaana, M. Holmström, A. Bhardwaj, and K. Asamura (2012), Energetic neutral atom observations of magnetic anomalies on the lunar surface, *J. Geophys. Res.*, *117*, A07208, doi:10.1029/2012JA017553.

Vorburger, A., P. Wurz, S. Barabash, M. Wieser, Y. Futaana, C. Lue, M. Holmström, A. Bhardwaj, M. Dhanya, and K. Asamura (2013), Energetic neutral atom imaging of the lunar surface, *J. Geophys. Res. Space Physics*, *118*(7), 3937–3945, doi:10.1002/jgra.50337.

Wang, X.-D., et al. (2010), Acceleration of scattered solar wind protons at the polar terminator of the Moon: Results from Chang'E-1/SWIDs, *Geophys. Res. Lett.*, *37*, L07203, doi:10.1029/2010GL042891.

Wieser, M., S. Barabash, Y. Futaana, M. Holmström, A. Bhardwaj, R. Sridharan, M. Dhanya, P. Wurz, A. Schaufelberger, and K. Asamura (2009), Extremely high reflection of solar wind protons as neutral hydrogen atoms from regolith in space, *Planet. Space Sci.*, *57*, 2132–2134, doi:10.1016/j.pss.2009.09.012.

Wurz, P., U. Rohner, J. A. Whitby, C. Kolb, H. Lammer, P. Dobnikar, and J. A. Martín-Fernández (2007), The lunar exosphere: The sputtering contribution, *Icarus*, *191*, 486–496, doi:10.1016/j.icarus.2007.04.034.

Zhang, H., K. K. Khurana, M. G. Kivelson, V. Angelopoulos, W. X. Wan, L. B. Liu, Q.-G. Zong, Z. Y. Pu, Q. Q. Shi, and W. L. Liu (2014), Three-dimensional lunar wake reconstructed from ARTEMIS data, *J. Geophys. Res. Space Physics*, *119*, 5220–5243, doi:10.1002/2014JA020111.